cene (*9*) shows that no equilibrium in the carbon cycle is established and that the waxing and waning of the terrestrial biosphere, possibly related to subtle climate variations and early human land use, are the most important factors controlling atmospheric CO_2 concentrations over the last 10,000 years.

During further glaciation in MIS 5.4, CO_2 concentrations remain constant, although temperatures strongly decline. We suggest that this reflects the combination of the increased oceanic uptake of CO_2 expected for colder climate conditions and CO_2 release caused by the net decline of the terrestrial biosphere during the glaciation and possibly by respiration of organic carbon deposited on increasingly exposed shelf areas. These processes, however, should terminate (with some delay) after the lowest temperatures are reached in MIS 5.4 and ice volume is at its maximum at 111 ky B.P. (*22*). In agreement with this hypothesis, CO_2 concentrations start to decrease in the Vostok record at about 111 ky B.P. Another possibility to explain this delayed response of CO_2 to the cooling during MIS 5.4 would be an inhibited uptake of CO_2 by the ocean. In any case, about 5°C lower temperatures on the Antarctic ice sheet during MIS 5.4 (*17*) are difficult to reconcile with the full interglacial CO_2 forcing encountered at the beginning of this cold period and again question the straightforward application of the past CO_2-climate relation to the recent anthropogenic warming.

Another scenario is encountered during MIS 7, in which no prolonged warm period is observed. Although temperatures at the end of termination III are comparable to those at the end of termination II and CO_2 concentrations are even slightly higher, a much shorter lag in the decrease of CO_2 relative to the Antarctic temperature decrease in MIS 7.4 is found. Comparison with the SPECMAP record (*23*) shows that during the preceding interglacial MIS 7.5, ice volume was much larger than during the Holocene and the Eemian warm periods. Accordingly, the buildup of the terrestrial biosphere during MIS 7.5 is expected to be much less and sea level changes smaller, leading to a smaller net release of CO_2 into the atmosphere during the following glaciation, which is not able to fully counterbalance the CO_2 uptake by the ocean.

References and Notes

1. J. M. Barnola, D. Raynaud, Y. S. Korotkevich, C. Lorius, *Nature* **329**, 408 (1987).
2. A. Neftel, E. Moor, H. Oeschger, B. Stauffer, *ibid.* **315**, 45 (1985).
3. D. Raynaud *et al.*, *Science* **259**, 926 (1993). Recent investigations in central Greenland have reported an in situ production of CO_2 in the ice, possibly related to carbonate or organic species reactions (or both), and have strongly compromised the validity of the determined CO_2 concentrations. However, Antarctic ice cores are (if at all) much less affected by this effect because of the very low abundance of reactive carbon species dissolved in Antarctic ice.
4. C. D. Keeling, T. P. Whorf, M. Wahlen, J. van der Pflicht, *Nature* **375**, 666 (1995).
5. M. Leuenberger, U. Siegenthaler, C. C. Langway, *ibid.* **357**, 488 (1992).
6. H. J. Smith, H. Fischer, M. Wahlen, D. Mastroianni, B. Deck, in preparation.
7. C. Lorius, J. Jouzel, D. Raynaud, J. Hansen, H. Le Treut, *Nature* **347**, 139 (1990).
8. M. Wahlen, D. Allen, B. Deck, A. Herchenroder, *Geophys. Res. Lett.* **18**, 1457 (1991). Air samples were extracted from Vostok 5G and TD ice with a dry extraction technique, and CO_2 concentrations were determined with laser spectroscopy. The accuracy of a single measurement (as essentially determined by the standard deviation of multiple frequency tunings of the diode laser) is better than 5 ppmv. The laser spectroscopic method enables the use of very small samples (~4 g), allowing us to pick crack-free ice and to measure replicate samples at the same depth interval. In general, all given CO_2 concentrations correspond to the average and standard deviation of at least three replicate samples. On average, the variability of such replicate measurements is 7.5 ppmv (1σ).
9. A. Indermühle *et al.*, *Nature*, in press.
10. J. Schwander *et al.*, *J. Geophys. Res.* **98**, 2831 (1993).
11. J.-M. Barnola, P. Pimienta, D. Raynaud, Y. S. Korotkevich, *Tellus Ser. B* **43**, 83 (1991).
12. Expanded ice age and air age time scales were kindly provided by J. Jouzel and J.-R. Petit. Ages were assigned to sample depths after slight depth corrections for the Vostok 5G core (*17*) by linear interpolation of the depth-age scale. A publication describing the calculation of the expanded time scales, which is essentially based on the procedure described by J. Jouzel *et al.* [*Nature* **364**, 407 (1993)], is in preparation.
13. T. Blunier *et al.*, *Nature* **394**, 739 (1998).
14. E. J. Steig *et al.*, *Science* **282**, 92 (1998).
15. A. Neftel, H. Oeschger, T. Staffelbach, B. Stauffer, *Nature* **331**, 609 (1988).
16. B. Stauffer *et al.*, *ibid.* **392**, 59 (1998).
17. J. Jouzel *et al.*, *Clim. Dyn.* **12**, 513 (1996).
18. J. R. Petit *et al.*, *Nature* **387**, 359 (1997).
19. S. J. Johnsen, W. Dansgaard, H. B. Clausen, C. C. Langway Jr., *ibid.* **235**, 429 (1972).
20. Phase relations were determined by comparison of maxima and minima in the long-term trend of CO_2 concentrations and isotope temperatures as represented by spline approximations. Given errors reflect the uncertainty in the actual positions of the extrema, which are weakly dependent on the degree of smoothing. They do not take into account the uncertainty in Δage. This additional error is treated separately in the discussion of the data.
21. T. Blunier *et al.*, *Geophys. Res. Lett.* **24**, 2683 (1997).
22. D. G. Martinson *et al.*, *Quat. Res.* **27**, 1 (1987).
23. J. Imbrie *et al.*, in *Milankovitch and Climate*, A. Berger *et al.*, Eds. (Reidel, Hingham, MA, 1984), pp. 269–305.

24. We thank J.-M. Barnola and D. Raynaud for helpful comments and for sharing with us their unpublished Vostok CO_2 record of the last four glacial-interglacial cycles during our sample selection process. This study was funded by NSF grants OPP9615292, OPP9196095, and OPP9118534. Financial support of H.F. has been provided by Deutsche Forschungsgemeinschaft.

30 November 1998; accepted 29 January 1999

Present-Day Deformation Across the Basin and Range Province, Western United States

Wayne Thatcher,[1]* G. R. Foulger,[2] B. R. Julian,[1] J. Svarc,[1] E. Quilty,[1] G. W. Bawden[1]

The distribution of deformation within the Basin and Range province was determined from 1992, 1996, and 1998 surveys of a dense, 800-kilometer–aperture, Global Positioning System network. Internal deformation generally follows the pattern of Holocene fault distribution and is concentrated near the western extremity of the province, with lesser amounts focused near the eastern boundary. Little net deformation occurs across the central 500 kilometers of the network in western Utah and eastern Nevada. Concentration of deformation adjacent to the rigid Sierra Nevada block indicates that external plate-driving forces play an important role in driving deformation, modulating the extensional stress field generated by internal buoyancy forces that are due to lateral density gradients and topography near the province boundaries.

The northern Basin and Range province is an actively deforming intracontinental plateau lying between the stable blocks of the Sierra Nevada and the Colorado Plateau (Fig. 1). The province has extended (increased in area) by about a factor of 2 over the past ~20 million years (*1*, *2*), and extension continues with ongoing seismic activity and slip along numerous faults distributed across a zone ~800 km wide (*3*–*5*). Constraints on the internal deformation of the province are limited. Geologic studies delineate regions of Holocene and late Quaternary fault slip (*3*, *4*). Space geodetic measurements broadly define movements across the province (*6*–*8*), and

[1]U.S. Geological Survey, MS/977, Menlo Park, CA 94025, USA. [2]Department of Geological Sciences, University of Durham, Science Laboratories, South Road, Durham DH1 3LE, UK.

*To whom correspondence should be addressed. E-mail: thatcher@usgs.gov

local surveys map concentrated deformation in several seismically active zones (*9–11*). The detailed pattern is important because it defines the current seismic hazard, with regions of high velocity gradient having more frequent damaging earthquakes than regions of low gradient. In addition, the spatial pattern constrains the fundamental processes driving active continental deformation, suggesting that external plate motions are more important than internal buoyancy forces in deforming the province.

Here we show the detailed velocity field mapped from a dense Global Positioning System (GPS) network that spans the Basin and Range. The GPS network consists of 63 stations, most of which were occupied on 2 or more days during surveys in 1992, 1996, and 1998 (*12*). The velocity of each station relative to stable North America was determined (Fig. 1), and velocity magnitude and vector orientations were calculated (Fig. 2).

Several first-order features are immediately apparent from Figs. 1 and 2. First, deformation is strongly concentrated in two regions: the westernmost ~200 km and easternmost ~100 km of the network, with little internal deformation of the intervening ~500 km of the central Basin and Range. Locally high velocity gradients (Fig. 2A) are associated with fault zones near 111.8° (Wasatch fault), 113° (Drum Mountain fault), 117.9° [Central Nevada seismic zone (CNSZ)], and across a more diffuse zone of conjugate strike-slip and normal faults between 119.1° and 120.2° [Sierra Nevada transition zone (SNTZ)]. This pattern is broadly consistent with existing geologic, seismic, and space geodetic data. Reconaissance geologic mapping (*3*, *4*) and seismicity compilations (*5*) show evidence for Holocene fault slip and historical seismic activity in central Utah and western Nevada but for pre-Holocene slip

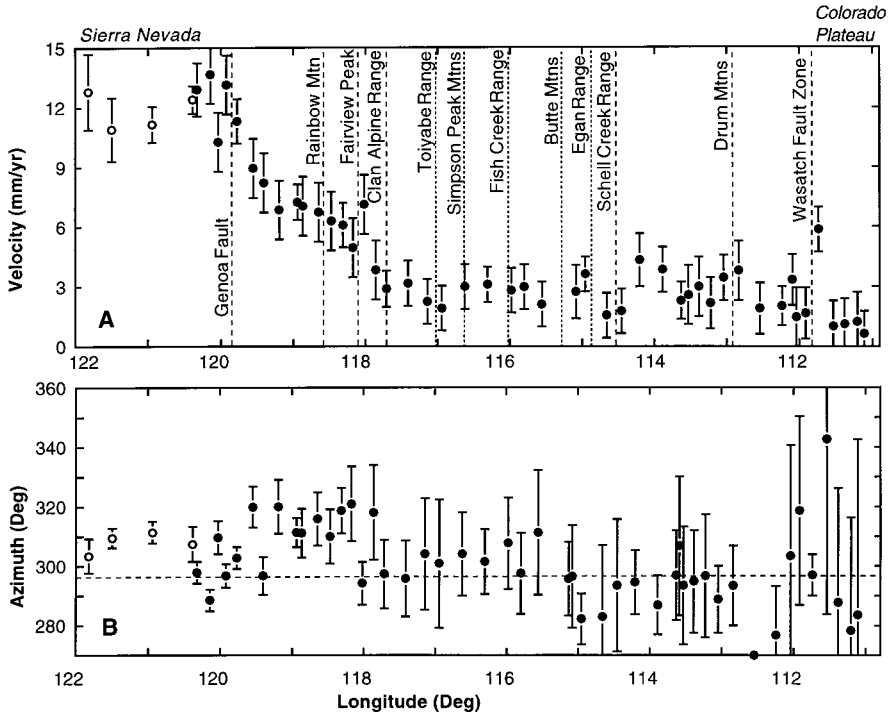

Fig. 2. Velocity magnitude (**A**) and azimuth measured clockwise from north (**B**) plotted versus longitude. Only the GPS stations along U.S. Highway 50 shown in Fig. 1 are plotted. However, the velocities of four additional continuously recording GPS stations (open circles) that lie within the stable Sierra Nevada block are shown for comparison. Error bars indicate 1 SD. Major range-bounding faults with Holocene slip (long-dashed lines) and Quaternary slip (short-dashed lines) are shown in (A), and the 308° azimuth of North America–Sierra Nevada relative motion (*13*) is shown by the horizontal dashed line in (B).

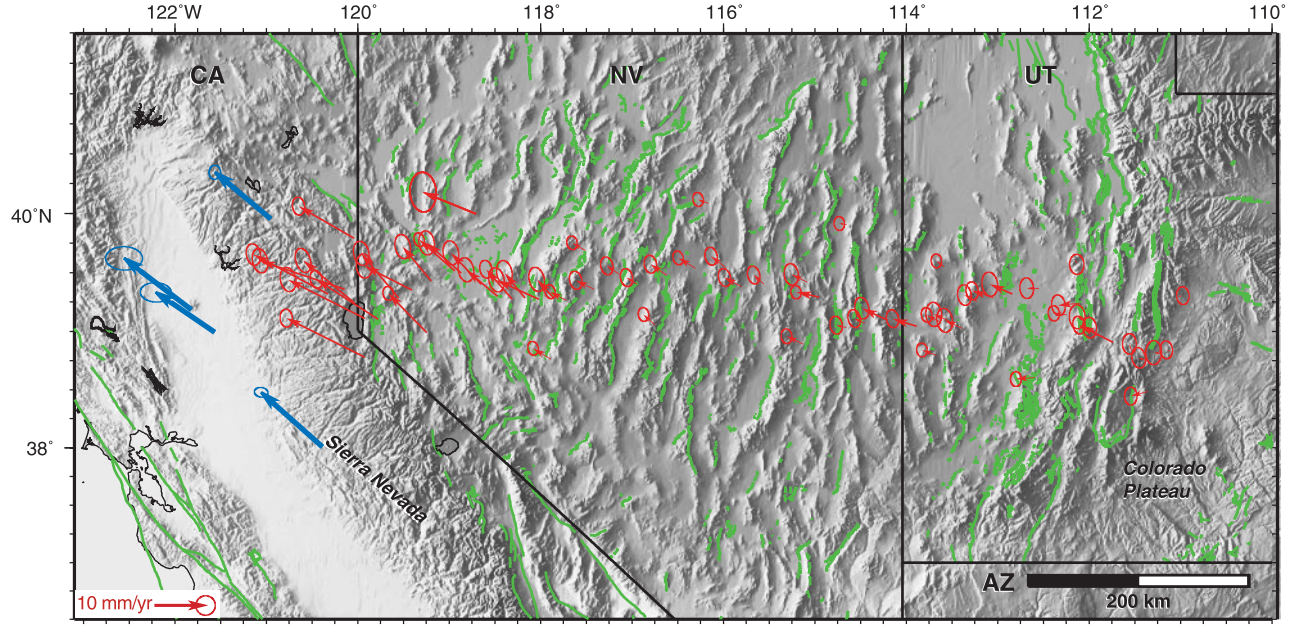

Fig. 1. GPS station velocities relative to other stations on the stable North American plate lying to the east of the network shown here. One standard deviation error ellipses are shown for each vector (*27*). The base map is shaded topography derived from data from the U.S. Geological Survey digital elevation model. State boundaries (CA, California; NV, Nevada; UT, Utah; AZ, Arizona) and stable blocks of the Sierra Nevada and Colorado Plateau are shown for reference. Active faults (*3*, *4*) are shown by solid green lines. The velocities of four stations on the stable Sierra Nevada block are shown with blue arrows. Velocities of Basin and Range stations are shown with red arrows.

and low seismicity levels in the central Basin and Range. Widely spaced VLBI (Very Long Baseline Interferometry) and continuous GPS station data are consistent with our results (*13*).

The distribution of deformation across western Nevada suggests that the 8 to 12 mm/year of ~310°-oriented relative motion across the eastern California shear zone (*7*, *14–16*), which lies south of our network near longitude 118°W, is partitioned between two fault zones. Average velocities of 2.8 ± 0.5 mm/year between 114.9° and 117.7°W increase to 6.5 ± 0.7 mm/year between 118° and 119.2°W and to 12.5 ± 1.5 mm/year between 119.9° and 120.2°W. Thus, 2.8 ± 0.5 mm/year of relative motion occurs across the Wasatch and related faults in central Utah, 3.7 ± 0.8 mm/year of relative northwestward motion occurs across the CNSZ, and an additional 6.0 ± 1.6 mm/year is accomodated within the SNTZ. The latter value is within the range of the ~3 to 6 mm/year of 300°-oriented motion inferred across faults in northwestern California and central Oregon (*17*), which suggests that much of this deformation may be accommodated through western Nevada.

Velocity vectors within the Basin and Range show the superposed effects of extensional stresses due to lateral density gradients in the lithosphere and tractions exerted by the relative motions of the bounding stable blocks. The average trend in velocity vector orientations across the province (Fig. 2B) is close to 310°, which is the direction of relative motion of the Sierra Nevada microplate with respect to stable North America (*6*, *7*, *13*), immediately suggesting the influence of this motion on internal deformation of the province. However, local variations in vector orientations provide clues that internal driving forces also affect the deformation.

The ~295° orientation of velocities in central Utah would seem to suggest deformation due largely to the motion of the Colorado Plateau (essentially stable North America) relative to the eastern Great Basin. However, the ~1-km increase in elevation and 15-km increase in crustal thickness across the Basin-Range/Colorado Plateau transition zone is expected to produce extensional stresses perpendicular to the Wasatch fault zone in central Utah (*18*). Geodetic measurements across the Wasatch zone are consistent with this stress field orientation. Velocity vectors and extensional strains are nearly normal to the local N20°E trends of the faults across our network (Fig. 1) and to the north-south–striking Wasatch zone near Ogden, 200 km farther north (*9*, *10*). These orientations are also consistent with least principal stress orientations inferred from various stress indicators near the Wasatch front (*19*).

Between 118° and 120°W, the orientation of velocities is within ±15° of the vector defining the relative motion of the Sierra Nevada block with respect to stable North America. This orientation, along with the high-velocity gradients across the region, suggest that Pacific plate–coupled motion of the Sierra Nevada microplate is responsible for much of the deformation of western Nevada. However, the large component of normal faulting present in this region suggests the perturbing influence of extensional stresses caused by buoyant, low-density, upper mantle beneath the Great Basin (*20*, *21*). The local 295° orientation of velocity vectors across the Sierra Nevada–bounding Genoa fault, a pure dip-slip north-south–striking normal fault near 120°W, may be due to the perturbing effects of stresses generated by topographic gradients across this transition zone (*18*). These stresses would tend to rotate velocity vectors toward the normal to the Genoa fault in the elevated Sierra Nevada and away from this direction in the lower lying Basin and Range, as observed.

The velocity field measured across active faults provides estimates of fault slip rate and constraints on the mechanism of elastic strain buildup in the adjacent crustal blocks (*22*). An elastic half-space dislocation model with a normal fault dipping 60° that does not slip between the surface and some fixed depth (H) but slides freely at a constant slip velocity below that depth yields the horizontal velocity expected due to elastic strain accumulation across the fault (*23*) (Fig. 3). The locked zone depth is taken to be the depth to which seismic fault slip or small earthquake hypocenters extend, which is 10 to 20 km in the Basin and Range. The high-velocity gradient in the model is ~3 H wide, or 30 to 60 km for locking depths that are appropriate here. For the area covered by our network, the expected pattern of horizontal velocity across an individual fault is thus well represented by a smoothed step and local peak or trough, with the net offset equal to the horizontal component of the fault slip rate. Strain accumulation across a series of widely spaced faults should resemble an irregular staircase, with steps being the zones of elastic strain accumulation and flats representing the intervening undeformed blocks.

The observed pattern of deformation across most of Nevada is similar to these expectations, with high-velocity gradients near 118° and 119.6°W and nearly constant velocities elsewhere. Figure 4 shows that bur-

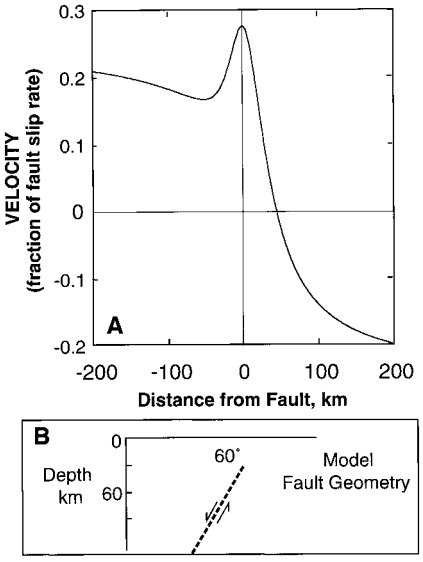

Fig. 3. (**A**) Horizontal velocity (west motion positive) versus distance for a fault model like that used in Fig. 4 to match velocity patterns across faults in Nevada. Horizontal distance is in kilometers perpendicular to the surface projection of a two-dimensional, 60°, west-dipping normal fault. The vertical axis gives the horizontal velocity component perpendicular to the fault normalized by the slip rate on the fault. (**B**) Model fault geometry.

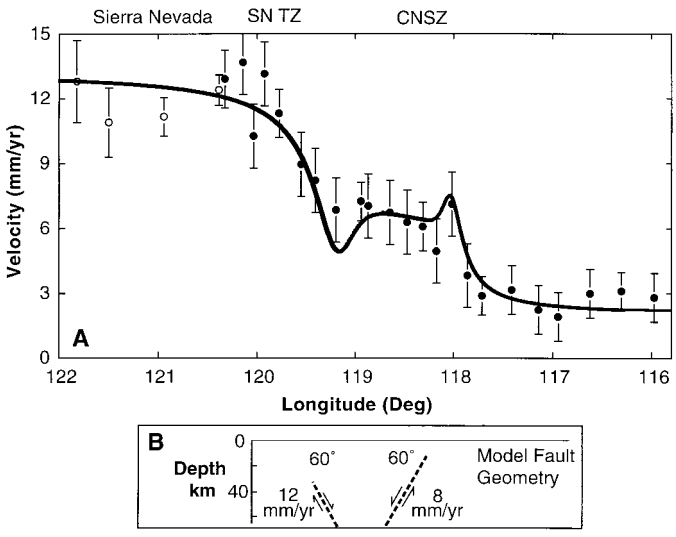

Fig. 4. (**A**) Observed velocities (circles as in Fig. 2A with 1-SD error bars) compared with the model calculation (solid curve) plotted versus longitude. The model includes two 60° dipping faults. One is inclined to the west beneath the CNSZ and slips at 8 mm/year. The other dips to the east beneath the SNTZ and slips at 12 mm/year. (**B**) Model fault geometry.

ied faults beneath the CNSZ and SNTZ can explain the main features of the data. Both normal and right-lateral strike-slip faulting occur across each zone, so the modeled fault slip rate is the resultant of these two components. Because a number of active faults are exposed at the surface in each zone, the models are undoubtedly oversimplified. For example, the SNTZ contains both strike- and dip-slip faults, and the width of the deforming zone suggests that several subparallel faults locked to ~10 to 15 km would match the data at least as well as a single fault locked to 30 km.

Movements in central Utah and eastern Nevada are more complex than those shown by the simple buried fault slip model. Horizontal velocities (Fig. 2A) increase near the Wasatch fault zone as expected but then abruptly decrease west of it. Velocity subsequently increases near the Drum Mountain faults, decreases to the west, and finally reaches a stable value of ~3 mm/year west of 113.3°W. There is suggestive evidence that a local velocity decrease similar to those shown in central Utah occurs near the Schell Creek Range [at 114.6° (Fig. 2A)]. The changes there are small, about 2 mm/year, and are supported by very few observations. However, it may be noteworthy that this is the only mapped Holocene fault that crosses our network between the Utah-Nevada border and the central Nevada seismic zone (*4*). Models like those in Fig. 3 match general features of the Utah and eastern Nevada data (*24*) but cannot reproduce the near-fault variations, which may be due to changes in slip along the fault strike (*25*).

Our results suggest that forces exerted on the Basin and Range by motions of the bounding plates are more important than internal buoyancy forces in driving large-scale deformation. Mappings of the gravitational potential energy that is available to cause deformation (*21*) show high gradients in eastern Nevada that do not correlate with strain rate gradients obtained by us. It may be that the stresses implied by these mappings are supported by the local strength of the lithosphere, with little resulting deformation. In contrast, the concentration of deformation near the western edge of the province indicates an important role for boundary forces due to motion of the Sierra Nevada microplate. Crustal thickness variations near the province boundaries may be important in causing deformation near the Wasatch fault and in complementing plate drag forces near the Sierra Nevada. However, the effects of all driving forces may be substantially modulated by lateral variations in lithospheric rheology, which is the relation between applied forces and the resulting displacements. Rheology is very sensitive to temperature and rock type (*26*), so we might expect that the varied structural and thermal history of the western United States would generate strong lateral variations in strength, channeling deformation into zones that are intrinsically weaker than their surroundings.

References and Notes

1. W. Hamilton, in *Continental Extensional Tectonics*, M. P. Coward, J. F. Dewey, P. L. Hancock, Eds. (Geological Society, London, 1987), vol. 28, pp. 155–176.
2. B. Wernicke, in *The Cordilleran Orogen: Conterminous U. S.: The Geology of North America Volume G-3*, P. W. Lipman, B. C. Burchfiel, M. L. Zoback, Eds. (Geological Society of America, Boulder, CO, 1992), pp. 553–581.
3. S. Hecker, "Quaternary tectonics of Utah with emphasis on earthquake-hazard characterization" (Bulletin 127, Utah Geological Survey, Salt Lake City, UT, 1993).
4. J. C. Dohrenwend, B. A. Schell, C. M. Menges, B. C. Moring, M. A. McKittrick, "Reconaissance photogeologic map of young (Quaternary and late Teritary) faults in Nevada" (Open-File Report 96-2, Nevada Bureau of Mines and Geology, Reno, NV, 1996).
5. D. M. dePolo and C. M. dePolo, "Earthquakes in Nevada 1852–1996" (Map 111, Nevada Bureau of Mines and Geology, Reno, NV, 1998).
6. D. F. Argus and R. G. Gordon, *Geology* **19**, 1085 (1991).
7. T. H. Dixon, S. Robaudo, J. Lee, M. C. Reheis, *Tectonics* **14**, 755 (1995).
8. R. A. Bennett, B. P. Wernicke, J. L. Davis, *Geophys. Res. Lett.* **25**, 563 (1998).
9. L. J. Martinez, C. M. Meertens, R. B. Smith, *ibid.*, p. 567.
10. J. C. Savage, M. Lisowski, W. H. Prescott, *J. Geophys. Res.* **97**, 2071 (1992).
11. J. C. Savage, M. Lisowski, J. L. Svarc, W. K. Gross, *ibid.* **100**, 20257 (1995).
12. The October 1992 survey was carried out with Turborogue GPS receivers with choke-ring antennas, and the September 1996 and September 1998 measurements were carried out with Ashtech Z12 receivers and Ashtech choke-ring antennas. The network consists of 47 stations strung about 15 to 30 km apart along U.S. Highway 50 and 16 stations spaced between 60 and 120 km apart to the north and south. The 16 bounding network stations and 8 additional Highway 50 stations were generally occupied on 4 consecutive days in each survey. Of the other Highway 50 sites, 23 were occupied on 2 consecutive days and the remaining 16 were observed on a single day. Most Highway 50 sites used National Geodetic Survey leveling benchmarks installed as long ago as 1932. Other sites used stainless steel plugs we cemented into bedrock outcrops. Data were reduced with Gipsy software release 4. Station positions for each epoch were derived in the ITRF96 reference frame, and velocity vectors were determined relative to stable North America. All station coordinates and site velocities may be accessed at the U.S. Geological Survey Web site (http://quake.wr.usgs.gov/QUAKES/geodetic/gps/).
13. The VLBI-derived estimate of Sierra Nevada–stable North America relative motion near 37°N, 118°W is 12.1 ± 1.2 mm/year at an azimuth of 322° ± 5° (*7*). The average of GPS determinations from four stations within the Sierra Nevada block (open circles in Fig. 2) is 11.8 ± 1.6 mm/year at 308° ± 5°. Values between 119.8° and 120.3°W average 12.5 ± 1.5 mm/year at 299° ± 5°. The velocity of a VLBI station near Ely, NV, is 4.9 ± 1.3 mm/year at an azimuth of 262° ± 13° (*7*). The VLBI site lies roughly equidistant and ~12 km from two of our stations [near 115°W (Fig. 2)] whose average velocity is 3.2 ± 1.6 mm/year at 303° ± 19°. Although the two estimates are consistent at the 2 SD level, our results from other GPS stations in the region suggest that velocities are generally directed more northwest and are smaller in magnitude than the nearly west-oriented value determined for the Ely VLBI site. Initial results from a 13-station continuous GPS array (*8*) located north of our network and roughly centered on 40°N show an increase in velocity west of the central Nevada seismic zone, which is consistent with our data. An inferred linear east-to-west increase in the east component of velocity (*8*) is not supported by our data. Instead, our data show an abrupt increase of east and north velocity components near 118°W.
14. R. K. Dokka and C. J. Travis, *Tectonics* **9**, 311 (1990).
15. J. Sauber, W. Thatcher, S. Solomon, *J. Geophys. Res.* **91**, 12683 (1986).
16. J. C. Savage, M. Lisowski, W. H. Prescott, *Geophys. Res. Lett.* **17**, 2113 (1990).
17. S. K. Pezzopane and R. J. Weldon, *Tectonics* **12**, 1140 (1993).
18. Isostatically balanced lateral differences in topography result from lateral density gradients that generate horizontal forces capable of causing deformation. For a two-dimensional structure across which the difference in topographic elevation is h and isostatic compensation occurs entirely within the crust, the force per unit length, F, normal to the structure is given by

$$F = \rho_c g h \{ y_{cco} + \frac{\rho_m h}{\rho_m - \rho_c} \}$$

where ρ_c is crustal density, ρ_m is mantle density, g is the gravitational acceleration, and y_{cco} is the crustal thickness of the low-lying region. If y_{cco} = 35 km, ρ_m = 3300 kg m^{-3}, ρ_c = 2750 kg m^{-3}, and h = 1 km, then $F = 2 \times 10^{12}$ N m^{-1}, which is comparable to many plate-driving and resisting forces. This force produces extensional stress in the elevated region and compressional stress in the adjacent lower lying crust [see D. L. Turcotte, in *Mountain Building Processes*, K. J. Hsu, Ed. (Academic Press, London, 1982), pp. 141–146]. The magnitude of these forces will differ if lateral density contrasts extend into the mantle. For example, the driving force will be smaller than computed above if the mantle lithosphere is colder and denser beneath the Sierra Nevada and Colorado Plateau than it is beneath the Basin and Range.
19. We assume that principal stress orientations estimated from earthquake fault plane solutions, borehole elongations, and slip directions on faults are coincident with incremental principal strains determined by GPS. M. L. Zoback [*J. Geophys. Res.* **94**, 7105 (1989)] has estimated least principal stress orientations that are nearly east-west across the Wasatch fault near Ogden and N90°E to N120°E across our GPS network.
20. A. H. Lachenbruch and P. Morgan, *Tectonophysics* **174**, 39 (1990).
21. C. H. Jones, J. R. Unruh, and L. J. Sonder [*Nature* **381**, 37 (1996)] calculate that the driving force contribution of buoyant upper mantle in the northern Basin and Range (termed gravitational potential energy by them) averages 1.5 × 10^{12} N m^{-1}, which is comparable to the effects of province margin topography given in (*18*). However, these authors also point out significant uncertainties in the computed force gradients due to poor constraints on the exact upper mantle density structure and its lateral variations.
22. J. C. Savage and R. O. Burford, *J. Geophys. Res.* **78**, 832 (1973); J. C. Savage, *ibid.* **88**, 4984 (1983).
23. L. B. Freund and D. M. Barnett, *Bull. Seismol. Soc. Am.* **66**, 667 (1976). The horizontal displacement pattern in Fig. 3 is for a west-dipping fault. If the fault has an eastward dip, the pattern is reversed, with all local peaks replaced by troughs and vice versa (turn Fig. 3 upside down to visualize this). For dips shallower than 60°, the local peaks and troughs become progressively less prominent for the same slip distribution as that in Fig. 3.
24. The central Utah models use two 60°-dipping faults locked from the surface to a depth of 15 km. Slip of 4 mm/year is required across the Wasatch fault and of 2 mm/year across the Drum Mountain fault. These slip rates are surprisingly high and may be related to a discrepancy noted from the Wasatch fault near Ogden, where geologically estimated late Holocene slip rates are 1 to 2 mm/year [D. P. Schwartz and K. J. Coppersmith, *J. Geophys. Res.* **89**, 5681 (1984)] and geodetic estimates are ~5 mm/year (*9*, *10*).
25. Some of the local velocity decreases seen at fault crossings of our network may be due to a sampling bias. Both coseismic fault slip and topographic height

are expected to be a maximum near the center of each range and to decrease toward its ends. The interseismic strain accumulation rate (the velocity gradient normal to the fault) should generally mimic this pattern. Because highway engineers site roadways through the lowest available topographic gradient, most of our range-crossing stations are located either near the ends of active ranges or between adjacent ones. This bias will produce local along-strike velocity gradients and velocity minima near the ends of active ranges, which is qualitatively consistent with patterns seen in our data across central Utah and easternmost Nevada.

26. W. F. Brace and D. L. Kohlstedt, *J. Geophys. Res.* **85**, 6248 (1980); L. J. Sonder and P. C. England, *Earth Planet. Sci. Lett.* **77**, 81 (1986).
27. Errors were assigned assuming station-day position uncertainties of 3 mm (north), 5 mm (east), and a random walk component of benchmark motion of 1 mm per (year)$^{1/2}$ [J. Langbein and H. Johnson, *J. Geophys. Res.* **102**, 591 (1997)].
28. This work was supported by NASA's Dynamics of the Solid Earth Program. Help with GPS fieldwork was provided by G. Hamilton, J. Sutton, C. Stiffler, G. Marshall, R. Stein, K. Hodgkinson, M. Hofton, N. King, T. Sagiya, and B. Kilgore. Discussion with W. Hamilton, A. H. Lachenbruch, T. Parsons, W. H. Prescott, J. C. Savage, R. Simpson, G. Thompson, R. Wells, and M. L. Zoback is gratefully acknowledged. Careful reviews of the manuscript were provided by J. C. Savage, M. L. Zoback, R. B. Smith, and an anonymous reviewer.

2 November 1998; accepted 27 January 1999

A Search for Companions to Nearby Brown Dwarfs: The Binary DENIS-P J1228.2-1547

E. L. Martín,[1] W. Brandner,[2] G. Basri[1]

Hubble Space Telescope imaging observations of two nearby brown dwarfs, DENIS-P J1228.2-1547 and Kelu 1, made with the near-infrared camera and multiobject spectrometer (NICMOS), show that the DENIS object is resolved into two components of nearly equal brightness with a projected separation of 0.275 arc second (5 astronomical units for a distance of 18 parsecs). This binary system will be able to provide the first dynamical measurement of the masses of two brown dwarfs in only a few years. Upper limits to the mass of any unseen companion in Kelu 1 yield a planet of 7 Jupiter masses aged 0.5 × 10^9 years, which would have been detected at a separation larger than about 4 astronomical units. This example demonstrates that giant planets could be detected by direct imaging if they exist in Jupiter-like orbits around nearby young brown dwarfs.

Brown dwarfs (BDs) are "failed stars"; that is, they are not massive enough to sustain stable hydrogen burning but are sufficiently massive to start deuterium burning (*1*). Brown dwarfs are more like giant planets than stars in that their luminosity and temperature drop continuously with time, and ultimately they become extremely cool and faint. The borderline between stars and BDs is estimated to be at about 0.075 solar mass ($M_\odot$) for solar metallicity (*2*). The deuterium burning limit is at a mass of about 13 M_J, where M_J denotes a Jupiter mass (~0.001 $M_\odot$) (*3*). We adopt this mass to separate BDs from planets in order to avoid the problems of a definition based on poorly understood formation mechanisms (*4*). For many years, BDs have eluded firm detection, but since 1995 several objects have been shown to be unambiguously substellar (*5, 6*). The evidence for BDs is based on observations of lithium (*7*), luminosity, and surface temperatures (*8*). However, no direct mass measurement of a brown dwarf has been obtained to date. We present here the first object for which this can be done in the near future.

The first free-floating BD discovered in the solar neigborhood was Kelu 1. It was found in a proper motion survey (*9*). The second nearby free-floating BD was discovered by the Deep Near-Infrared Survey (DENIS). The DENIS and 2MASS surveys are ongoing and have the aim of yielding a complete sky coverage in the near-infrared *I*, *J*, and *K′* bands (*10*). The analysis of only 220 square degrees (about 1% of the planned DENIS survey) provided three objects (*11*) with *I*-*J* colors redder than GD 165B, which was the coolest BD candidate known before the discovery of Gl 229B (*12*). The surface temperatures of Kelu 1 and the DENIS objects are not obviously low enough to establish a substellar status, because young BDs and very low-mass stars can have the same effective temperature. The necessary distinctive substellar signature came from the spectroscopic detection of lithium in the atmospheres of Kelu 1 and DENIS-P J1228.2-1547 (hereafter abbreviated as DENIS 1228-15). (*13*). On the other hand, in very low-mass stars, the temperature and pressure at the bottom of the convection zone are high enough so that lithium gets rapidly destroyed through proton capture. The combination of high lithium abundance with low surface temperature implies that Kelu 1 and DENIS 1228-15 must have masses lower than 0.065 $M_\odot$ and ages younger than 10^9 years (1 Gy) (*13*).

We observed DENIS 1228-15 and Kelu 1 with NICMOS camera 1 (NIC1) on the Hubble Space Telescope (HST). The NIC1 data of DENIS 1228-15 were obtained on 2 June 1998 in multiple-accumulate mode with filters F110M, F145M, and F165M (*14*). This instrumental configuration provides an optimal combination of throughput and spatial resolution. Our observations of Kelu 1 were obtained using the same configuration on 14 August 1998. The NIC1 images of DENIS 1228-15 resolved two components of similar brightness (Fig. 1). To estimate the parameters of this binary system, we used an iterative approach: We modeled the data assuming two point sources and using both model and observed point spread functions (PSFs). The positions and the brightness ratios of the two point sources were free parameters, and the iterations continued until the residuals were similar to the noise. We obtained a separation of 0.275 ± 0.002 arc sec and a position angle of 41.0 ± 0.2°. The apparent F110M, F145M, and F165M magnitudes (respectively) on the HST-Vega system (*15*) are as follows: DENIS 1228-15 A (15.69, 14.96, and 13.98); DENIS 1228-15 B (15.89, 15.12, and 14.13); and Kelu 1 (14.13, 13.23, and 12.37). The standard deviation of these magnitudes is less than 0.01 magnitude, but the systematic errors can be up to 0.1 magnitude. Our F165M magnitude of 12.37 for Kelu 1 is in agreement with the published *H* magnitude of 12.32 (*9*). The B/A flux ratio of the DENIS 1228-15 system increases toward longer wavelength (0.83 for F110M, 0.86 for F145M, and 0.87 for F165M), indicating that DENIS 1228-15 B is slightly cooler than DENIS 1228-15 A. An independent confirmation of the binary nature of DENIS 1228-15 comes from public HST/NIC3 observations with filter F187N obtained on 24 June 1998 for another program by Hugh Jones and Todd Henry. The scale of NIC3 of 0.2 arc sec/pixel undersamples the PSF (theoretical full width at half maximum of 0.16 arc sec at 1.87 mm). Within the uncertainties due to the undersampling, the fitted values for the NIC3 data are in agreement with the results derived from the NIC1 data.

The trigonometric parallaxes of DENIS 1228-15 and Kelu 1 are not yet known, although they can be obtained with ground-based telescopes (*16*). The distance to Kelu 1

[1]Department of Astronomy, University of California, Berkeley, CA 94720, USA. [2]Jet Propulsion Laboratory/Infrared Processing and Analysis Center, Mail Code 100-22, Pasadena, CA 91125, USA.